Journal of Civil Engineering and Architecture 19 (2025) 266-278
doi: 10.17265/1934-7359/2025.06.002

Peak Wind Force Coefficients of Porous Panels Mounted on the Roofs of High-Rise Buildings

Tomoko Aihara[1] and Yasushi Uematsu[2]

1. Taisei Advanced Center of Technology, TAISEI CORPORATION, Yokohama 245-0051, Japan

2. New Industry Creation Hatchery Center, Tohoku University, Sendai 980-8579, Japan

Abstract: Wind tunnel experiment and CFD (computational fluid dynamics) simulation with LES (large eddy simulation) have been conducted to investigate the characteristics of peak wind force coefficients of porous panels mounted on the roofs of high-rise buildings. First, aerodynamic modelling of porous panels was discussed. The relation between pressure loss coefficient and porosity was obtained. Then, a wind tunnel experiment was conducted to measure the wind forces (net wind pressures) acting on solid and porous panels mounted on the roof of a high-rise building. Because it was difficult to measure the pressures on both sides of thin, porous panel at the same location simultaneously, we proposed to use the roof edge pressures near the panel for the panel's inside-surface pressures. This experimental method was validated by a CFD simulation reproducing the wind tunnel experiment. The characteristics of peak wind force coefficients of porous panels mounted on the roofs of high-rise buildings were made clear. Finally, positive and negative peak wind force coefficients for designing the rooftop porous panels were proposed.

Key words: Rooftop panel, porosity, peak wind force coefficient, wind tunnel experiment, CFD, LES.

1. Introduction

Panels are usually installed on the rooftops of buildings so that rooftop equipment and others are not visible from the outside. Hence, they are called blindfold panels. Porous panels are often used to cool the equipment by wind. Although the wind force coefficients for designing ground-mounted porous panels are specified in building codes and standards, e.g., Building Standard Law of Japan [1], those for roof-mounted porous panels are not specified. This is due to lack of data. It is difficult to fabricate the model of thin, porous panel and to measure the wind pressures on both sides of the panel in wind tunnel experiments.

Regarding the wind loads on building components similar in shape to rooftop blindfold panels, Stathopoulos et al. [2] measured local and area-averaged wind pressures on parapets of flat-roof buildings. The height of the parapet model was 5 or 10 mm (1 or 2 m at full scale). The results indicated that the parapet height did not affect the critical design loads significantly. The authors discussed problems related to the assumption of considering the roof edge pressure as acting on the inside surface of the parapet. They found that combination of peak wind pressure coefficients on the wall and roof edges overestimated the wind loads on parapets, particularly in diagonal winds.

Japanese researchers have investigated the wind loading of blindfold panels mounted on the rooftops of middle-rise and high-rise buildings (see, Ohtake [3], Honda et al. [4], Tagawa et al. [5]). Itoh et al. [6] measured peak wind force coefficients on a panel mounted on the rooftop of a high-rise building to obtain data for validating the CFD (computational fluid dynamics) simulation method employed in their study. However, all of these studies dealt with only solid panels with no porosity.

Corresponding author: Yasushi Uematsu, Dr. Eng., Senior Research Fellow, research fields: wind engineering, snow engineering, structural engineering and steel structure.

Porous materials are often used for ground-mounted windbreak fences. Eexperimental studies have been conducted using wind tunnels to clarify the characteristics of wind loads on such windbreak fences (e.g., Gandemer [7]). Wind loads on vertically elevated panels (e.g., signboards) with various porosities were measured by Letchford [8], Briassoulis et al. [9] and Giannoulis et al. [10]. Relationship between pressure loss coefficient and porosity for porous panels has been discussed by many researchers; a review of previous studies on this subject can be found in Xu et al. [11]. Recently, CFD simulations have been employed for investigating the wind loads on porous fences. Reproduction of the configuration of solid obstacles in fine mesh discretization is a direct way to make numerical calculations on porous objects. However, computations using such a fine mesh increase computational time and load significantly. Therefore, a method called “pressure jump” or “porous jump” is often used, in which a pressure loss is applied to the interface of the computational cell; see Tominaga and Shirzadi [12], for example. Maruyama [13] applied space averaging to the Navier-Stokes equations and derived filtered equations with a SGS (subgrid-scale) turbulence modeling for LES (large eddy simulation).

The present paper proposes a method for estimating the net wind forces on porous blindfold panels mounted on the rooftops of high-rise buildings in a wind tunnel. The aerodynamic modelling of porous panels is based on the porosity and pressure loss coefficient of the material. The wind pressures on the panel’s outside surface are measured directly, while the nearby rooftop pressures are used in place of the wind pressures on the panel’s inside surface. Such an experimental method is validated by a CFD simulation with LES, in which the porous panel is faithfully reproduced using a fine mesh. Then, the characteristics of the maximum (positive) and minimum (negative) peak wind force coefficients of the panels are investigated based on the results of the wind tunnel experiment and the CFD simulation. Finally, positive and negative peak wind-force coefficients for designing the porous rooftop panels are proposed.

2. Aerodynamic Modelling of Porous Panels

Many kinds of porous materials are used for rooftop blindfold panels. Among them, the present paper focuses on planar materials such as perforated metal with many small holes; blind fences such as louvers are not considered here. It is difficult to fabricate wind tunnel models of such porous panels at the same geometric scale as the building. Thus, we focus on the porosity ϕ and pressure loss coefficient ζ of the panel. Table 1 summarizes the dimensions of the models used in the present study. They are made of 0.2 mm thick brass plates using an etching manufacturing. The porosity ϕ is adjusted by changing the dimensions of the square holes (W, P, d). The pressure loss coefficient ζ of each panel is measured by using a small wind tunnel with a circular cross section of 125 mm diameter (see Fig. 1). Fig. 2 shows the ζ-ϕ relation, in which the results for porous panels with circular holes [14] are also plotted for a comparative purpose. The results for both hole configurations agree well with each other. The relation between ζ and ϕ is approximated by $\zeta = 0.38\phi^{-2.9}$ (solid line in Fig. 2). Similar relations were obtained by Xu et al. [11] and Tominaga et al. [12].

Table 1 Characteristics of the model panels.

No.	ϕ (%)	Dimensions (mm)			Notation
		W	P	d	
1	20	1	2.24	1.24	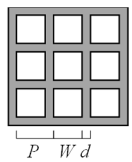
2	20	2	4.47	2.47	
3	20	3	6.71	3.71	
4	50	1	1.41	0.41	
5	50	2	2.83	0.83	
6	50	3	4.24	1.24	
7	80	2	2.24	0.24	
8	80	3	3.35	0.35	

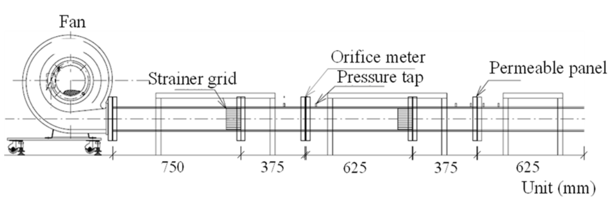

Fig. 1 Wind tunnel for measuring pressure loss coefficient.

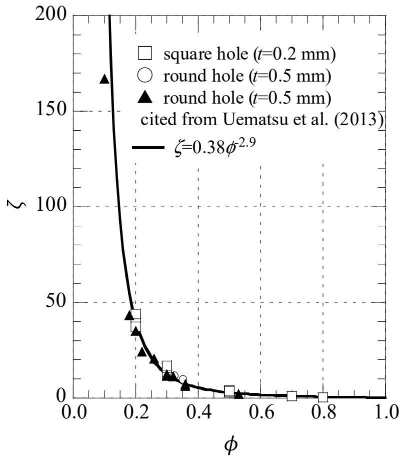

Fig. 2 Relation between ζ and ϕ.

3. Investigated Building and Wind Tunnel Model

The subject of this study is porous blindfold panels installed along the rooftop perimeter of a high-rise building. The breadth B, depth D and height H of the building are 30 m, 30 m, and 90 m, respectively. The height of the blindfold panels is 6 m. The wind tunnel model is made at a geometric scale of λ_L = 1/300. Fig. 3 shows the dimensions of the model together with the location of pressure taps on the roof and panel (only outside surface). The details of the porous panels with ϕ = 20% and 50% (Models 3 and 6) are shown in Fig. 4. Fig. 5 is a close-up view of the roof with panels of ϕ = 50%. Because the net wind force on the panel is provided by the difference between wind pressures on the outside and inside surfaces of the panel, it is necessary to install pressure taps on both sides at the same location. However, such an installation is impossible in practice. Thus, seven pressure taps of 1 mm inside diameter are installed only on the outside surface of the panel placed on Side A (see Fig. 3). The pressure taps are located at approximately the mid-height of the panel. The tap height from the rooftop is 10 mm for ϕ = 0%, 9.8-11.4 mm for ϕ = 20%, 8.8-10 mm for ϕ = 50%, and 9.8-11.5 mm for ϕ = 80%. The pressure taps are installed on the solid parts of the panel for ϕ = 20%. On the other hand, they are installed in the center of holes for ϕ = 50% and 80%. The pressure tubes are led into the building model at 15 mm from the roof edge. Thus, a part of each pressure tube is exposed outside the model, which may affect the flow around the panel depending on the wind direction. The pressure taps on the roof are located 5 mm from the roof edge. The wind pressures at these rooftop taps are used in place of the wind pressures on the panel's inside surface. The pressure taps are connected to differential pressure transducers via 800 mm lengths of vinyl tubes of 1.4 mm inside diameter.

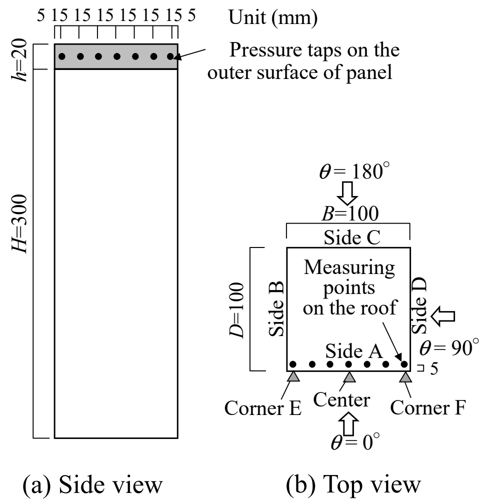

Fig. 3 Dimensions of the experimental model.

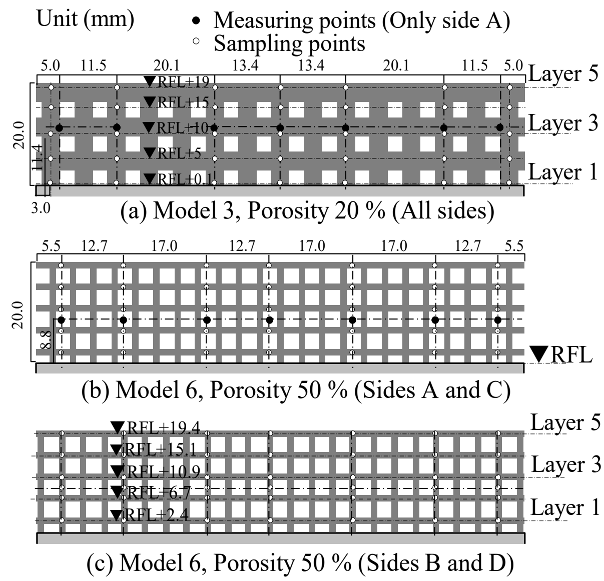

Fig. 4 Location of measuring points (experiment) and sampling points (CFD).

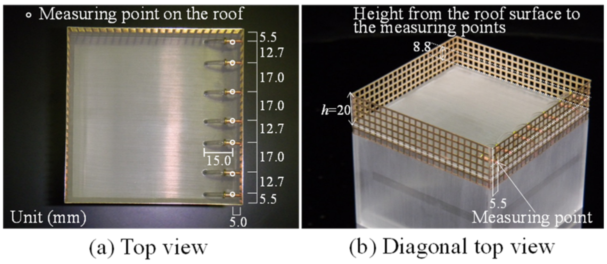

Fig. 5 Close-up view of an experimental model (ϕ = 50%).

4. Experimental Procedure

The experiment was carried out in a turbulent boundary layer developed over the floor of an Eiffel-type wind tunnel with a working section 2.0 m wide, 1.5 m high and 11.0 m long. Fig. 6 shows the profiles of mean wind speed U_z, normalized by the value at a height of H (= 300 mm), and turbulence intensity I_z at the center of the building model with no model in place. The solid lines in the sub-figures represent the profiles of U_z and I_z for Terrain Category III (suburban exposure), specified in the AIJ-RLB (AIJ Recommendations for Loads on Buildings) [15]. The reduced power spectrum $fS(f)/\sigma^2$ of wind speed fluctuation at a height of H is shown in Fig. 7, where $S(f)$ = power spectrum, f = frequency, σ = standard deviation of wind speed fluctuation, and L_x = integral scale of turbulence. The general shape of $S(f)$ is consistent with the Karman-type spectrum with L_x = 43.4 cm, which roughly corresponds to the specified value in the AIJ-RLB [15] when λ_L = 1/300.

In the experiment, the mean wind speed U_H at the roof height H was set to 13.5 m/s. The velocity scale (λ_V) of the wind tunnel flow was assumed to be 1/3, resulting in the time scale (λ_T) of 1/100. The wind direction θ, defined as shown in Fig. 3b, was varied from 0° to 180° at an increment of 10°. Two additional wind directions of θ = 45° and 135° were also considered. The wind pressures at all pressure taps on the panel (outside) and roof were sampled at a sampling frequency of 1,000 Hz during a sampling period of 33 s, corresponding to 50 min at full scale, from which 5 sets of full-scale 10-min time histories of wind pressures were obtained. The wind pressures were

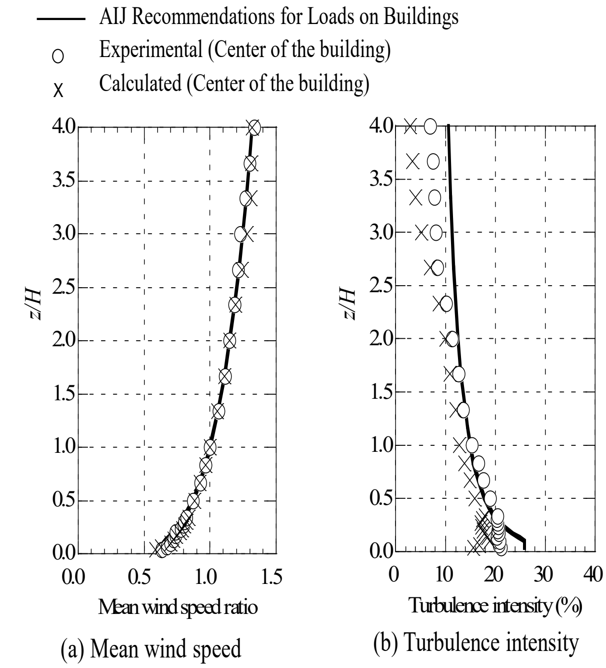

Fig. 6 Profiles of mean wind speed and turbulence intensity.

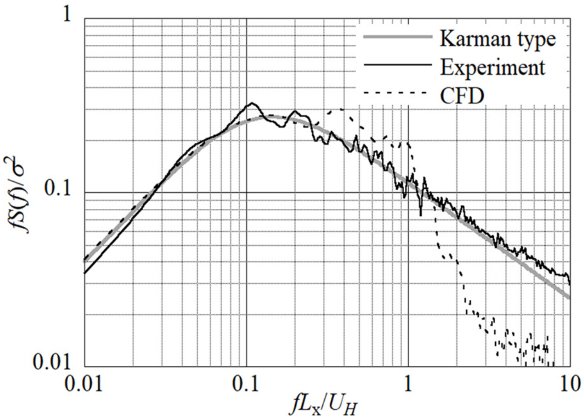

Fig. 7 Reduced power spectrum of wind speed fluctuation.

normalized by the mean velocity pressure q_H (= $0.5\rho U_H^2$, with ρ being the air density) of the approach flow at the roof height H to produce wind pressure coefficients. The wind force coefficient C_f on the panel is provided by the difference between wind pressure coefficients, C_{pe} and C_{pi}, on the outside and inside surfaces of the panel. In the experiment, C_{pi} was replaced by the wind pressure coefficient C_{pr} at the nearby pressure tap on the roof. The averaging time for evaluating the peak wind pressure and wind force coefficients was 0.5 s at full scale. The maximum and minimum peak values of wind pressure and wind force coefficients during a period of 10 min at full scale were obtained by applying ensemble averaging to the results of consecutive 5 runs. The Reynolds number *Re*, defined by $Re = U_H D/\nu$, with ν being the kinematic viscosity of air, was about 9×10^4. The blockage ratio *Br*, defined by the ratio of the model's vertical cross-sectional area to that of the wind tunnel was about 1.4% at most. The values of Re and Br in the present experiment satisfy the requirements of the ASCE Wind Tunnel Testing for Buildings and Other Structures [16], i.e., $Br < 5\%$ and $Re > 1.1 \times 10^4$.

5. Outline of CFD Simulation

The CFD simulation reproduces the wind tunnel experiment with a geometric scale of $\lambda_L = 1/300$, in which LES is employed. Solid panel ($\phi = 0\%$) and porous panels with $\phi = 20\%$ (Model 3) and 50% (Model 6) are considered. Fig. 8 shows the test models. The governing equations for the object under consideration are the continuity equation and the Navier-Stokes equations. The FVM (finite volume method) is used as the discretization method. A standard Smagorinsky model is used for the SGS turbulence model. The Smagorinsky constant C_s is set to 0.15. Unstructured grids composed of mainly tetrahedral elements are used for the computational grids.

The dimension of the computational domain is $30B$ (length) × $20B$ (width) × $15B$ (height). The center of the building model is placed $8B$ from the inflow boundary. The boundary conditions are as follows: i.e., free slip for the side and top boundaries, advective outflow condition for the outlet boundary, and wall function for the surfaces of ground and building, where three layers of boundary meshes are inserted around the surfaces. The inflow turbulence is generated by a preliminary computation with spires and roughness blocks, as with the wind tunnel experiment. The characteristics of the generated turbulent boundary layer at the center of the building model with no model in place are compared with those of the wind tunnel flow in Figs. 6 and 7. The agreement between wind tunnel experiment and CFD simulation is good for the mean wind speed profile (Fig. 6). The values of turbulence intensities I_z are somewhat smaller than the experimental ones. However, the agreement is relatively good for $z/H < 2$. The non-dimensional power spectrum of wind speed fluctuation at the roof height H is shown in Fig. 7. The value of L_x is 36 cm, which is slightly smaller than that of the wind tunnel flow (= 43.4 cm). Due to a filtering effect of the grid, the simulated power spectrum is smaller than the Karman-type spectrum in a high reduced-frequency range, such as $f \cdot L_x/U_H > 1.5$, for example. However, the shape of the power spectrum in the lower reduced-frequency range agrees with the Karman type spectrum, which is important for the wind load estimation by CFD simulation.

The building model, including the panels, is faithfully reproduced using a fine grid. However, the pressure tubes exposed outside the model are not reproduced. The mesh divisions in the whole area and around the porous panel with $\phi = 20\%$ are illustrated in Fig. 9. The maximum grid size is B in the upper zone, while the minimum grid size is $B/512$ ($\approx W/15$) near the porous panel. The mesh division was determined with reference to Yoshikawa and Tamura [17, 18]. The total number of elements is about 5.7, 7.4 and 9.5 million for $\phi = 0\%$, 20% and 50%, respectively.

The wind directions tested in the CFD simulation are 0°, 45° and 70° for $\phi = 0\%$, and 0° and 45° for $\phi = 20\%$ and 50%; these wind directions generate larger wind forces on the panels. The location of sampling

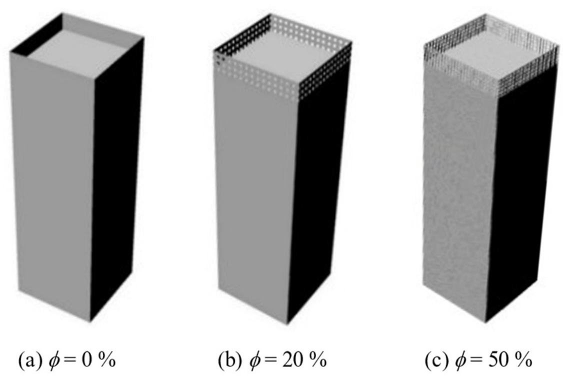

Fig. 8 Test models for CFD simulation.

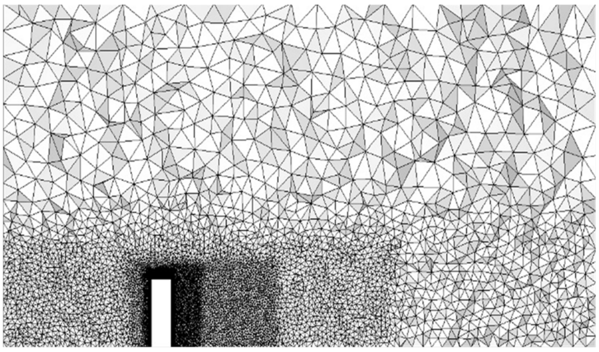

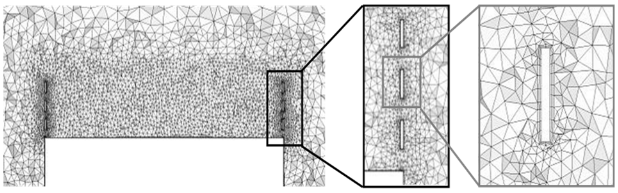

Fig. 9 Grid system for simulating the model (vertical section).

points of wind pressures is shown by open circles in Fig. 4. For models with ϕ = 0% and 20%, the wind pressures are sampled at approximately the same location of pressure taps on the wind tunnel models. In the cases of ϕ = 50% and 80%, the pressure taps are installed in the center of holes in the wind tunnel models, as mentioned above (see Fig. 4). In the CFD simulation, on the other hand, the sampling points are in the solid parts. When comparing the CFD simulation results for the wind pressure coefficients with the experimental ones at each pressure tap, the average of the values at the upper and lower points of the pressure tap is used. The time step of computation is 5×10^{-5} s (0.0036 s at full scale). The total number of steps is about 850,000, which corresponds to 50 min at full scale. The sampling frequency of pressure measurements is 2,000 Hz. The evaluation method for the peak wind pressure and wind force coefficients is the same as in the wind tunnel experiment.

6. Validation of the CFD Simulation

Both the CFD simulation and the wind tunnel experiment provide the wind pressure coefficients C_{pe} on the panel's outside surface and C_{pr} on the roof. Considering that the net wind force coefficient C_f (= C_{pe} - C_{pi}) on the panel is estimated by C_f^* = C_{pe} - C_{pr} in the wind tunnel experiment, comparisons between CFD simulation and wind tunnel experiment is made for C_{pe}, C_{pr} and C_f^* in order to validate the CFD simulation employed in the present study. Note that direct comparisons between CFD simulation and wind tunnel experiment can be made for these aerodynamic coefficients.

Figs. 10 and 11 show comparisons between CFD simulation and wind tunnel experiment for the statistical values of C_{pe}, C_{pr} and C_f^* for ϕ = 0% and 50%, respectively. The results obtained at all pressure taps and all wind directions are plotted in the figures. Good agreement between these two results can be seen; the CFD results are within approximately ±20% of the experimental ones. The agreement for ϕ = 50% is slightly worse than for ϕ = 0%. It was found that the larger the porosity of the panel, the greater the degree of discrepancy between CFD simulation and wind tunnel experiment tended to be. A detailed examination of the results indicates that the discrepancy is the greatest when θ = 135° or 180°, that is, when the wind blows against the wall on the opposite side of the instrumented panel. At these wind directions, the exposed pressure tubes exist on the windward side of the instrumented panel in the wind tunnel model (see Fig. 5a). Consequently, the flow around the panel may be affected by the pressure tubes. On the other hand, the exposed pressure tubes are not reproduced in the CFD simulation. Thus, it is thought that the discrepancy between CFD simulation and wind tunnel experiment is due to the exposed pressure tubes. Nevertheless, the agreement is good for wind pressure and wind force coefficients of large magnitude. This feature is important for practical design. It is concluded that the CFD simulation employed in the present study reproduces the wind tunnel experiment satisfactorily.

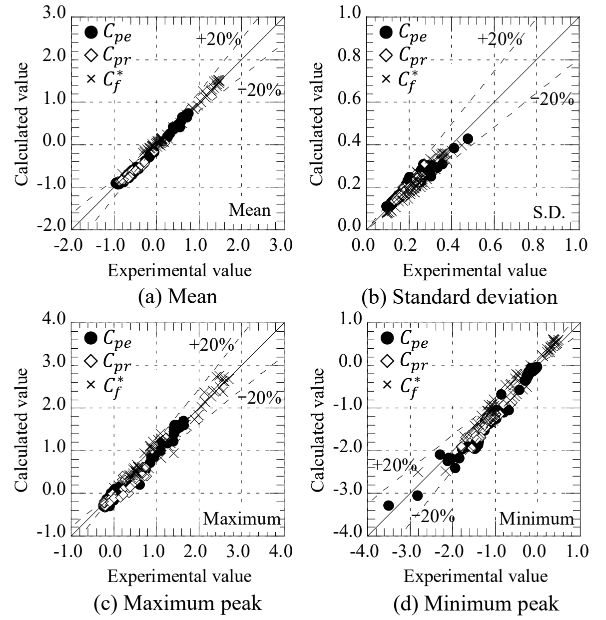

Fig. 10 Comparison between CFD simulation and wind tunnel experiment for the external pressure coefficients and wind force coefficients (ϕ = 0%).

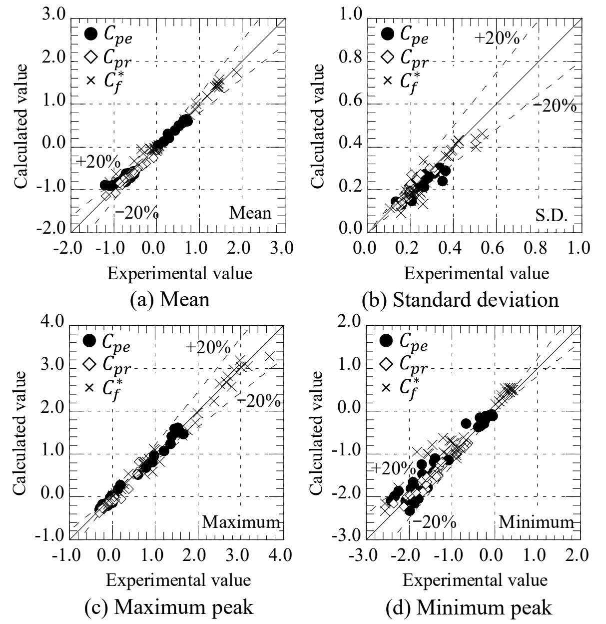

Fig. 11 Comparison between CFD simulation and wind tunnel experiment for the external wind pressure coefficients and wind force coefficients (ϕ = 50%).

7. Results and Discussion

7.1 Characteristics of the Maximum and Minimum Peak Wind Force Coefficients

Fig. 12 show the most critical maximum (positive) and minimum (negative) peak wind force coefficients irrespective of wind direction, $\hat{C}^*_{f\mathrm{cr}}$ and $\check{C}^*_{f\mathrm{cr}}$, at each measuring point, which are obtained from the wind tunnel experiment. In the figure, the wind directions, $\hat{\theta}_{\mathrm{cr}}$ and $\check{\theta}_{\mathrm{cr}}$, providing $\hat{C}^*_{f\mathrm{cr}}$ and $\check{C}^*_{f\mathrm{cr}}$ are also presented. The results are not necessarily symmetric with respect to the centerline of the panel, which may be due to non-uniformity of the flow and inevitable experimental errors. The largest value of $\hat{C}^*_{f\mathrm{cr}}$ occurs near Corner B at θ = 30°-45° (a diagonal wind). The larger ϕ, the larger the horizontal variation in $\hat{C}^*_{f\mathrm{cr}}$. On the other hand, the largest value of $|\check{C}^*_{f\mathrm{cr}}|$ occurs near Corner A at θ = 130°-140° (another diagonal wind) in most cases. Contrary to $\hat{C}^*_{f\mathrm{cr}}$, the larger ϕ, the smaller the horizontal variation in $\check{C}^*_{f\mathrm{cr}}$.

Based on these findings, focus is on the wind pressures on the panel and roof near the corners. It is thought that $\hat{C}^*_f$ is caused by a combination of positive C_{pe} and negative C_{pr} of large magnitude. Similarly, $\check{C}^*_f$ is thought to be caused by a combination of positive C_{pr} and negative C_{pe} of large magnitude. Fig. 13a shows the maximum peak value of C_{pe} (represented as $\hat{C}_{pe}$) and the minimim peak value of C_{pr} (represented as $\check{C}_{pr}$) near Corner B when θ = 45°. The results for the solid panel are also represented by the solid and dashed lines. The value of $\hat{C}_{pe}$ is minutely affected by ϕ. This feature implies that $\hat{C}_{pe}$ is primarily caused by the turbulence in the approach flow. On the other hand, the value of $\check{C}_{pr}$ increases in magnitude with an increase in ϕ. It is well accepted that peak suctions on the roof near the windward corner are caused by conical vortices in diagonal winds. In the case of solid panel, the conical vortices are generated away from the roof surface. Therefore, the effects of conical vortices on the roof pressures become small. By comparison, in the case of porous panels, the conical vortices are generated closer to the roof surface. The larger the porosity, the greater the effects of conical vortices on $\check{C}_{pr}$. As a result, $\hat{C}^*_f$ increases with an increase in ϕ. When the porosity is large, such as ϕ = 80%, for example, the wind passes through the porous panels,

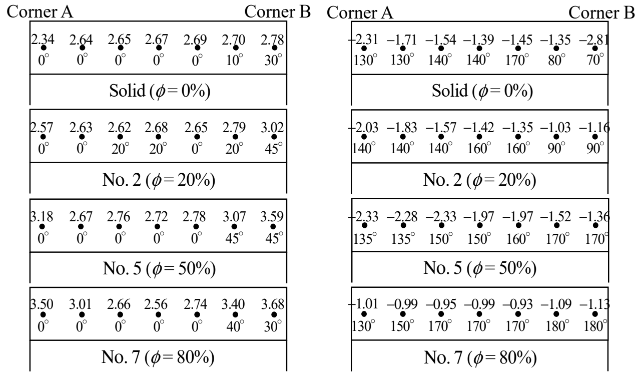

(a) $\hat{C}^*_{f\mathrm{cr}}$ and $\hat{\theta}_{\mathrm{cr}}$ (b) $\check{C}^*_{f\mathrm{cr}}$ and $\check{\theta}_{\mathrm{cr}}$

Fig. 12 The values of $\hat{C}^*_{f\mathrm{cr}}$ and $\check{C}^*_{f\mathrm{cr}}$ and the wind directions, $\hat{\theta}_{\mathrm{cr}}$ and $\check{\theta}_{\mathrm{cr}}$, providing them at each point.

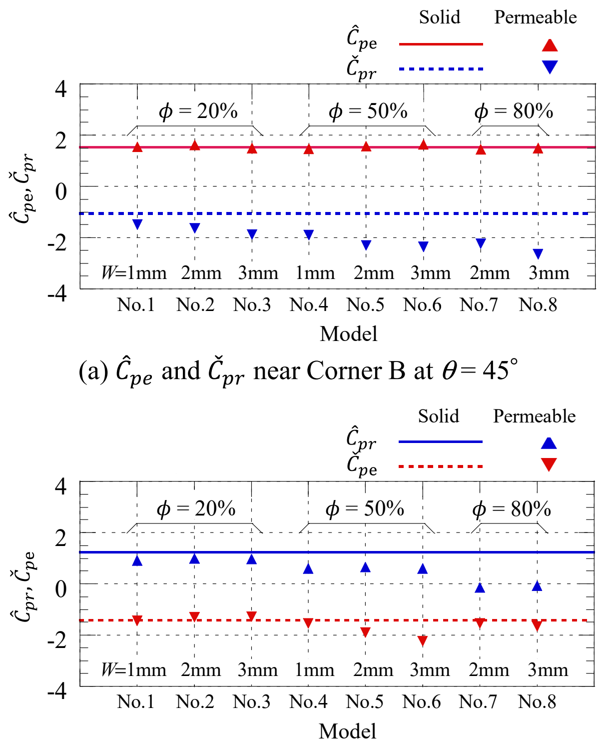

(a) $\hat{C}_{pe}$ and $\check{C}_{pr}$ near Corner B at θ = 45°

(b) $\hat{C}_{pr}$ and $\check{C}_{pe}$ near Corner A at θ = 135°

Fig. 13 Peak wind pressure coefficients on the roof and panel's outside surface.

and stronger conical vortices may be generated, resulting in larger suctions on the roof.

Next, Fig. 13b shows the maximum peak value of C_{pr} (represented as $\hat{C}_{pr}$) and the minimum peak value of C_{pe} (represented as $\check{C}_{pe}$) when θ = 135°. The $\hat{C}_{pr}$ value increases with decreasing ϕ. When ϕ is small, the air stagnates on the upwind side of the panel, generating large $\hat{C}_{pr}$ values. The $\check{C}_{pe}$ value is affected by ϕ only slightly. As a result, $\check{C}^*_f$ decreases in magnitude with increasing ϕ. These results indicate that the peak wind forces on the panel are dominated by the wind pressures on the panel's inside surface.

In practical design, *peak* + *peak* combination of wind pressure coefficients is often used for estimating design wind loads on panels, as mentioned above. That is, $\hat{C}^*_f$ and $\check{C}^*_f$ are estimated by "$\hat{C}_{pe}$ + $\check{C}_{pr}$" and "$\check{C}_{pe}$ + $\hat{C}_{pr}$", respectively. Table 2 shows a comparison between the exact values (Wind tunnel) and the *peak* + *peak* estimations for $\hat{C}^*_f$ and $\check{C}^*_f$. The estimated values are about 10% to 20% larger in magnitude than the exact values. This is because the peak values of C_{pe} and C_{pr} do not necessarily occur at the same time.

Figs. 14 and 15 respectively show the variation of the maximum and minimum peak wind force coefficients among seven measuring points (represented as $\hat{C}^*_{f\mathrm{all}}$ and $\check{C}^*_{f\mathrm{all}}$, respectively) with wind direction θ. Each subfigure shows the results for the same ϕ value. The results for solid panel (ϕ = 0%) are also represented by the dashed lines. The values of $\hat{C}^*_{f\mathrm{all}}$ in a wind direction range of θ = 0°-60° tend to increase with an increase in ϕ. The reason for this phenomenon was discussed above. It is interesting to note that the values of $\hat{C}^*_{f\mathrm{all}}$ depend on the panel model (i.e., hole dimensions) even if the porosity ϕ is the same. This feature suggests that the structure of conical vortices depends on the hole dimensions. However, the values of $\hat{C}^*_{f\mathrm{all}}$ for θ > 60° are minutely affected by ϕ. In the case of solid panel, the value of $\check{C}^*_{f\mathrm{all}}$ becomes the minimum (maximum in magnitude) at a wind direction

Table 2 Comparison between exact value by wind tunnel experiment and *peak* + *peak* estimation for $\hat{C}^*_f$ and $\check{C}^*_f$.

No.	$\hat{C}^*_f$ (Corner B, θ = 45°)		$\check{C}^*_f$ (Corner A, θ = 135°)	
	Wind tunnel	$\hat{C}_{pe} + \check{C}_{pr}$	Wind tunnel	$\check{C}_{pe} - \hat{C}_{pr}$
1	2.78	3.03	-2.17	-2.37
2	3.01	3.25	-2.01	-2.31
3	3.09	3.37	-1.98	-2.22
4	2.94	3.38	-1.86	-2.16
5	3.59	3.88	-2.33	-2.54
6	3.69	4.02	-2.55	-2.86
7	3.46	3.70	-0.98	-1.40
8	3.87	4.14	-1.38	-1.60

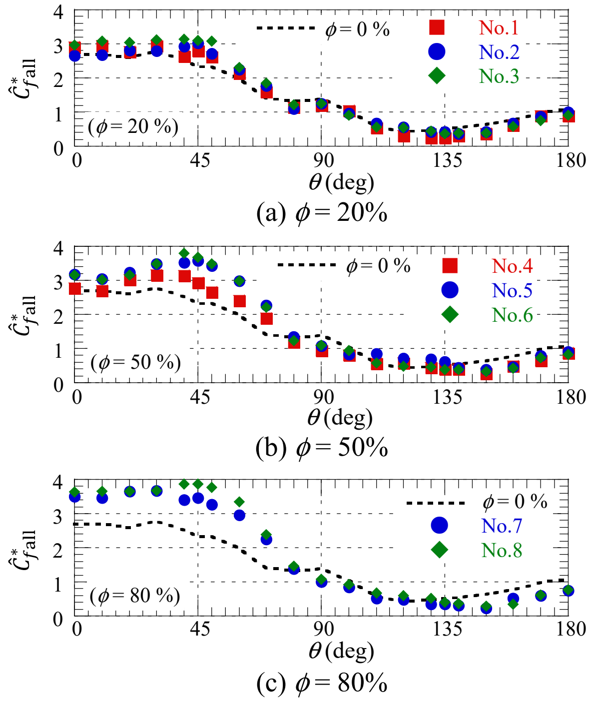

Fig. 14 Variation of $\hat{C}^*_{f\mathrm{all}}$ with wind direction θ.

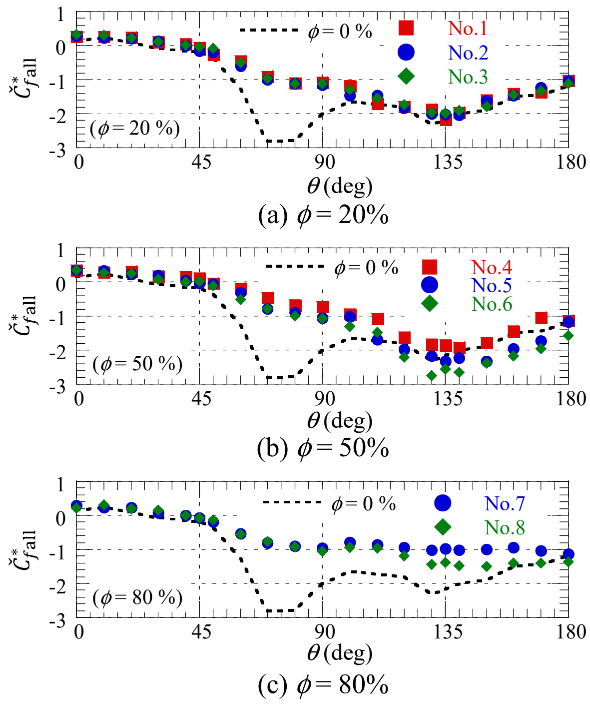

Fig. 15 Variation of $\check{C}^*_{f\mathrm{all}}$ with wind direction θ.

ranging from 70° to 80°. This is due to large suctions acting on the outside surface of the panel, which may be generated by a conical vortex near the top of the panel [19]. It is thought that the strength of this vortex weakens with an increase in ϕ. When $\phi \geq 20\%$, $\check{C}^*_{f\mathrm{all}}$ becomes the minimum at $\theta \approx 135°$. At this wind direction, the value of $\check{C}^*_{f\mathrm{all}}$ depends on the hole dimensions even if ϕ is the same. This feature is similar to that of $\hat{C}^*_{f\mathrm{all}}$ at $\theta \approx 45°$. In other wind directions, the effect of hole dimension on $\check{C}^*_{f\mathrm{all}}$ is small; the behavior of $\check{C}^*_{f\mathrm{all}}$ depends mainly on ϕ. The magnitude of $\check{C}^*_{f\mathrm{all}}$ in a range of θ = 90°-180° tends to decrease with an increase in ϕ, although the results for ϕ = 50% show slightly larger magnitude. As ϕ increases, the values of C_{pr} and C_{pe} approach each other due to pressure equalization, resulting in a decrease in the magnitude of $\check{C}^*_f$.

In the AIJ-RLB [14], the design wind load on cladding is given by the product of the mean velocity pressure q_H of the approach flow at the mean roof height H, peak wind force coefficient and subjected area A_c of cladding, and positive and negative peak wind-force coefficients, $\hat{C}_{f\_\mathrm{pos}}$ and $\hat{C}_{f\_\mathrm{neg}}$, are specified. The specified values of $\hat{C}_{f\_\mathrm{pos}}$ and $\hat{C}_{f\_\mathrm{neg}}$ are determined based on the mean values of the maximum and minimum peak wind force coefficients to account for their variations. Following such a procedure, we focus on the ensemble average of five data of the maximum or minimum peak wind-force coefficients obtained from the wind tunnel experiment.

7.2 Variation of the Maximum and Minimum Peak Wind Force Coefficients with Height

This section discusses the validity of substituting C_{pr} for C_{pi} based on the CFD simulation. The maximum and minimum peak values of C_{pi} at various wind directions are compared with those of C_{pr} for ϕ = 0%, 20% and 50% in Figs. 16-18, respectively. Focus is on Layer 5 (near the top), Layer 3 (approximately at the mid-height) and Layer 1 (near the roof). In the case of ϕ = 0% (Fig. 16), the agreement is generally good. However, when θ = 90° and 180°, the agreement is relatively poor at Layers 3 and 5 for the minimum peak pressure coefficients ($\check{C}_{pr}$ and $\check{C}_{pi}$).

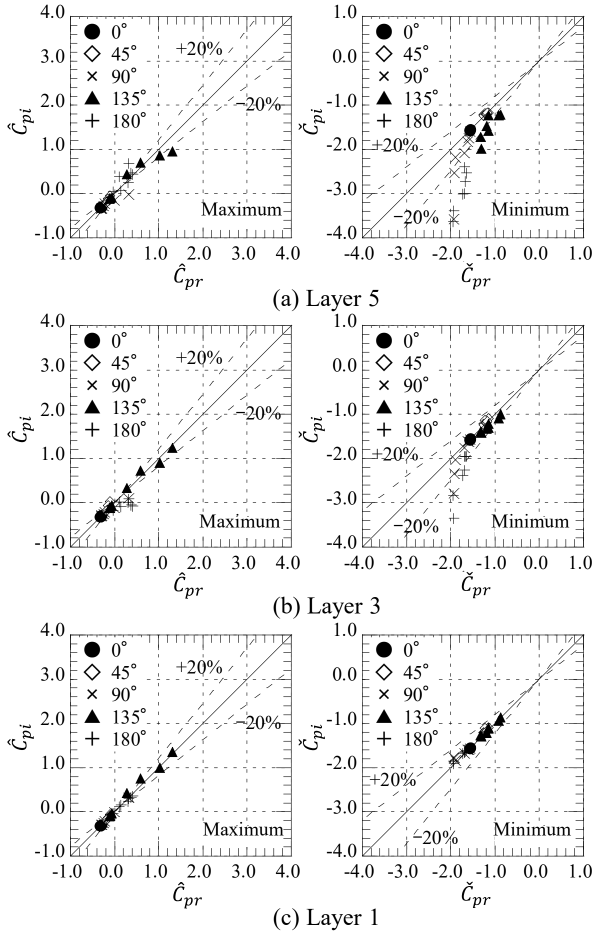

Fig. 16 Comparison between C_{pi} and C_{pr} for ϕ = 0%.

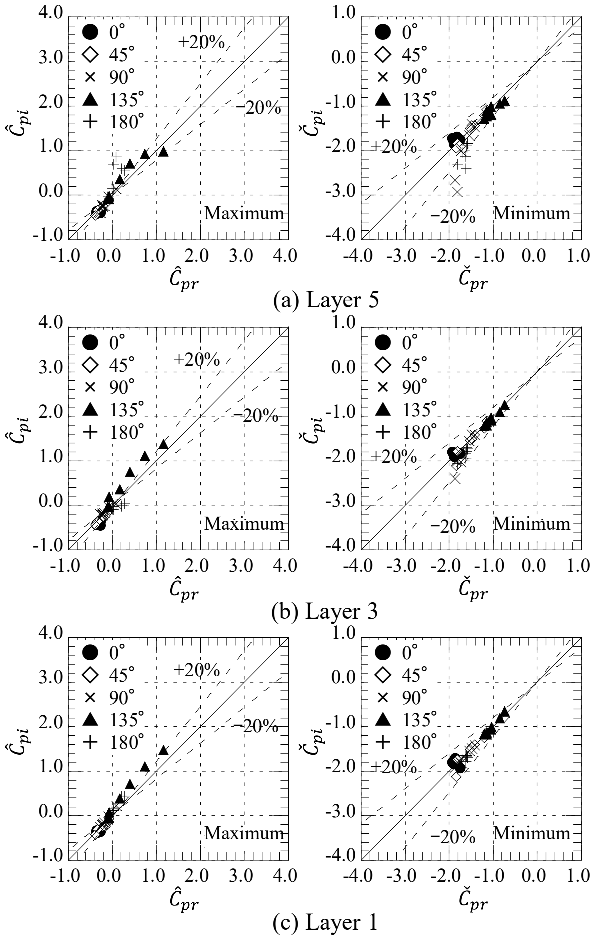

Fig. 17 Comparison between C_{pi} and C_{pr} for ϕ = 20%.

This is due to a large variation of $\check{C}_{pi}$ with height; $\check{C}_{pi}$ is larger in magnitude at higher layers. The largest discrepancy was found at the corner tap (see Fig. 3b). In the case of ϕ = 20% (Fig. 17), a similar feature as in the ϕ = 0% case can be seen for Layer 5. By comparison, the agreement is relatively good for Layer 3. It is thought that the pressure equalization due to panel's permeability smoothens the vertical variation of $\check{C}_{pi}$. In the case of ϕ = 50% (Fig. 18), the agreement is good even at Layer 5. However, the overall correlation between $\check{C}_{pr}$ and $\check{C}_{pi}$ is somewhat worse than in the case of ϕ = 20%. Because the porosity is so large that the correlation between $\check{C}_{pr}$ and $\check{C}_{pi}$ becomes worse, but the vertical distribution of $\check{C}_{pi}$ becomes more uniform. These results imply that the roof pressures near the panel can be used for estimating the net wind forces on panels with moderate porosities, such as ϕ = 20%-50%, for example. For panels with smaller porosities, such as ϕ < 20%, for example, the roof pressures underestimate the net wind forces on the panel at upper layers.

Figs. 19a, 19b and 19c show the variation of the maximum and minimum peak wind force coefficients among seven measuring points, $\hat{C}_{f\mathrm{all}}$ and $\check{C}_{f\mathrm{all}}$, at Layers 1, 3 and 5 with wind direction θ for ϕ = 0%, 20% and 50%, respectively. The CFD results are plotted by symbols (open circles and closed squares). The sampling points of pressure coefficients are represented by small open circles in Fig. 4. The experimental results ($\hat{C}^*_{f\mathrm{all}}$ and $\check{C}^*_{f\mathrm{all}}$) are shown by solid and dashed lines. As mentioned above, the experimental results are estimated by C_{pe} and C_{pr}. Furthermore, C_{pe} is measured at only one height (approximately at mid-height). It is found that the variation of $\hat{C}_{f\mathrm{all}}$ and $\check{C}_{f\mathrm{all}}$

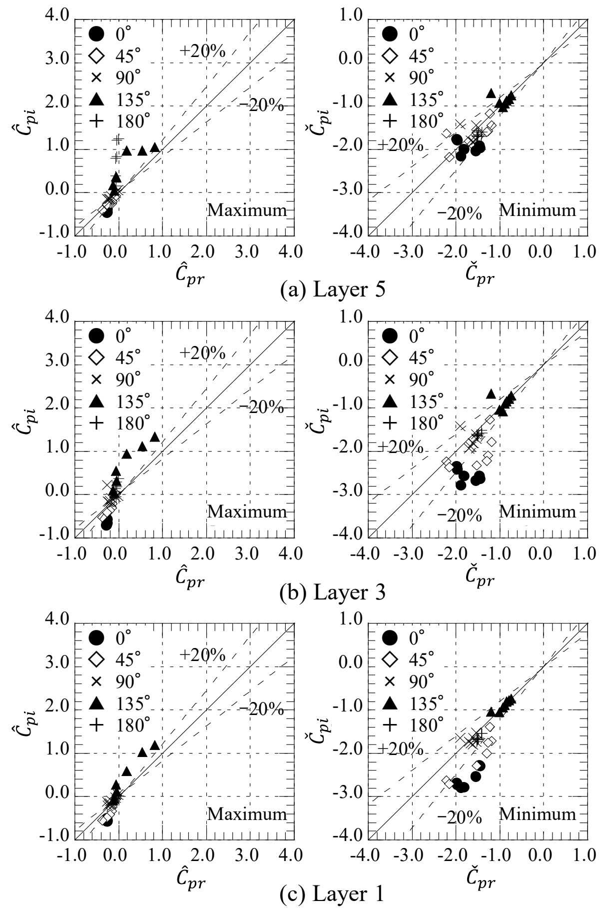

Fig. 18 Comparison between C_{pi} and C_{pr} for ϕ = 50%.

with height (layer) is relatively small. When ϕ = 0%, larger difference between CFD simulation and wind tunnel experiment can be seen for $\hat{C}_{f\mathrm{all}}$ and $\check{C}_{f\mathrm{all}}$ at higher layers when $\theta \approx$ 90°, 180° and 270°. This is due to negative C_{pi} values with large magnitude at higher layers. On the other hand, when ϕ = 20% and 50%, the agreement is generally good. This feature indicates that the experimental method employed in the present study can reasonably estimate the maximum and minimum peak wind force coefficients on porous panels with $\phi \geq$ 20%.

The values of ζ for porous panels with ϕ = 20%, 50% and 80% are about 0.4, 4 and 40, respectively (see Fig. 2). Despite such a large difference in ζ among panels, the maximum value of $\hat{C}_f$ among all points and all wind directions ranges from about 3 to 4, and the minimum value of $\check{C}_f$ among all points and all wind directions ranges from about -1 to -3. Despite such large changes in ζ and ϕ, the changes in $\hat{C}_f$ and $\check{C}_f$ are relatively small. In the design practice, the maximum and minimum peak wind force coefficients can be set as +4 and -3, respectively, on the safer side.

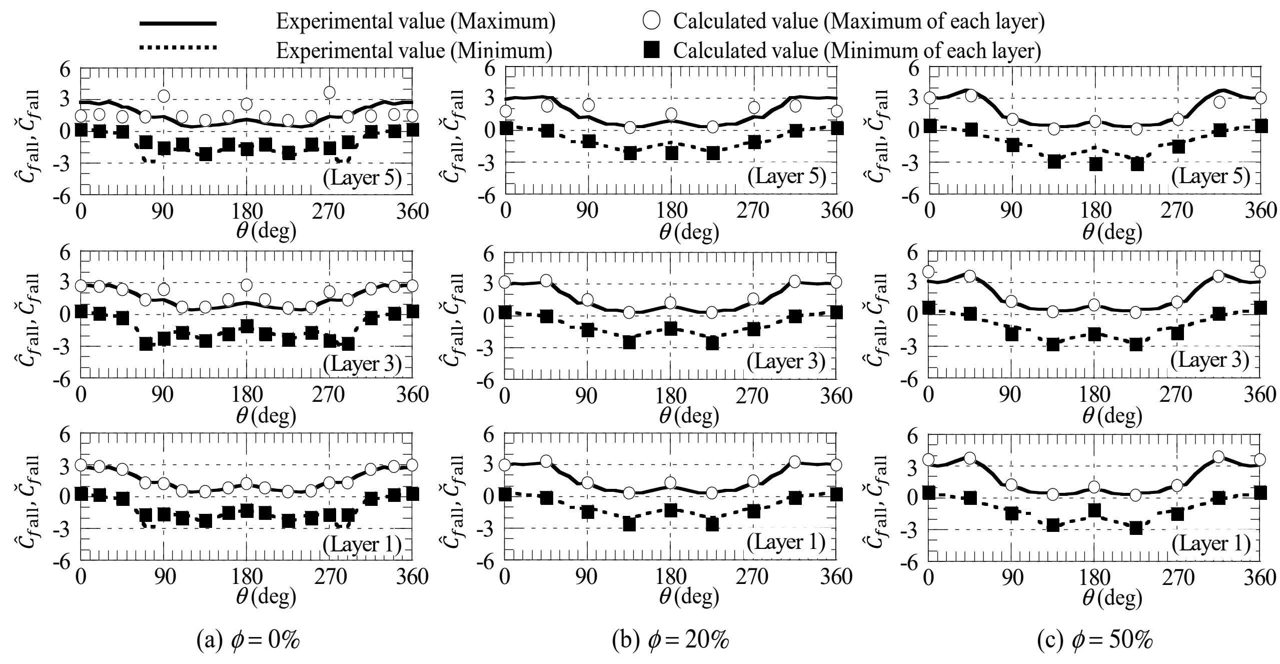

Fig. 19 Variation of $\hat{C}_{f\mathrm{all}}$ and $\check{C}_{f\mathrm{all}}$ with wind direction θ.

8. Concluding Remarks

Wind loads on 6 m high porous panels installed along the rooftop perimeter of a high-rise building (90 m high) have been investigated based on a wind tunnel experiment and a CFD simulation with LES. The porosity ϕ of the panel was changed from 0% (solid) to 80%. The main findings obtained from the present study may be summarized as follows:

(1) The variation of the maximum and minimum peak wind force coefficients with height is small when $\phi \geq$ 20%. Therefore, the roof edge pressures near the panel can be used for the pressures on the panel's inside surface for estimating the wind force coefficients on the panel.

(2) The peak wind force coefficient $\hat{C}_f$ becomes the largest near the windward corner in a diagonal wind ($\theta \approx$ 45°). The value increases with an increase in ϕ, which ranges from about 3 to 4.

(3) The minimum peak wind force coefficient $\check{C}_f$ becomes the largest in magnitude near the leeward corner in a diagonal wind ($\theta \approx$ 135°). The value tends to decrease in magnitude with an increase in ϕ, which ranges from about -1 to -3.

(4) The maximum and minimum peak wind force coefficients are less sensitive to the pressure loss coefficient ζ and porosity ϕ. In practical design, the maximum and minimum peak wind force coefficients can be set as +4 and -3, respectively, on the safer side.

References

[1] Information Center for Building Administration, Japan Building Disaster Prevention Association. 2020. *Commentary on structural regulations of the building standard law of Japan*. Tokyo: Japan Building Disaster Prevention Association. (in Japanese)

[2] Stathopoulos, T., Saathoff, P., and Du, X. 2002. "Wind Loads on Parapets." *Journal of Wind Engineering and Industrial Aerodynamics* 90: 503-14.

[3] Ohtake, K. 2008. "Peak Wind Pressure Coefficients for Cladding of a Large Roof." *Summaries of Technical Papers of Annual Meeting, Architectural Institute of Japan, Structures* I: 217-8. (in Japanese)

[4] Honda, H., Kurita, T., Katou, N., and Komi, T. 2015. "A Study of Peak Wind Force Coefficients for Screen Standing on Rooftop." *Summaries of Technical Papers of Annual Meeting, Architectural Institute of Japan, Structures* I: 185-6. (in Japanese)

[5] Tagawa, Y., Kikuchi, H., and Tamura Y. 2016. "Characteristics of Peak Wind Force Coefficients Acting on Rooftop." *Summaries of Technical Papers of Annual Meeting Architectural Institute of Japan, Structures* I: 215-6. (in Japanese)

[6] Itoh, Y., Kondo, K., Kikuchi, H., Nozu, T., Ohtake, K., Tanaka, H., Kawai, H., and Tamura, T. 2016. "Application of CFD Technique to Wind-Resistant Design of Buildings Part 2: Wind Tunnel Experiment for Office and Residential Type Tall Buildings." *Summaries of Technical Papers of Annual Meeting, Architectural Institute of Japan Structures* I: 235-6. (in Japanese)

[7] Gandemer, J. 1981. "The Aerodynamic Characteristics of Windbreaks, Resulting in Empirical Design Rules." *Journal of Wind Engineering and Industrial Aerodynamics* 7: 15-36.

[8] Letchford, C. W. 2001. "Wind Loads on Rectangular Signboards and Hoardings." *Journal of Wind Engineering and Industrial Aerodynamics* 89: 135-51.

[9] Briassoulis, D., Mistriotis, A., and Giannoulis, A. 2010. "Wind Forces on Porous Elevated Panels." *Journal of Wind Engineering and Industrial Aerodynamics* 98: 919-28.

[10] Giannoulis, A., Stathopoulos, T., Briassoulis, D., and Mistriotis, A. 2012. "Wind Loading on Vertical Panels with Different Permeabilities." *Journal of Wind Engineering and Industrial Aerodynamics* 107-108: 1-16.

[11] Xu, M., Patruno, L., Lo, Y.-L., and Miranda, S. 2020. "On the Use of the Pressure Jump Approach for the Simulation of Separated External Flows around Porous Structures: A Forward Facing Step." *Journal of Wind Engineering and Industrial Aerodynamics* 207: 104377.

[12] Tominaga, Y., and Shirzadi, M. 2022. "RANS CFD Modeling of the Flow around a Thin Windbreak Fence with Various Porosities: Validation Using Wind Tunnel Measurements." *Journal of Wind Engineering and Industrial Aerodynamics* 230: 105176.

[13] Maruyama, T. 2008. "Large Eddy Simulation of Turbulent Flow around a Windbreak." *Journal of Wind Engineering and Industrial Aerodynamics* 96: 1998-2006.

[14] Uematsu, Y., Sakurai, S., Miyamoto, Y., and Gavanski, E. 2013. "Wind Force Coefficients for Designing Porous Canopy Roofs." *Journal of Civil Engineering and Architecture* 7 (9): 1047-55.

[15] Architectural Institute of Japan. 2015. *Recommendations for Loads on Buildings*. Tokyo: Architectural Institute of Japan.

[16] American Society of Civil Engineers. 2012. *Wind Tunnel Testing for Buildings and Other Structures.* Reston, VA: ASCE/SEI 49-12.

[17] Yoshikawa, M., and Tamura, T. 2013. “Evaluation of Fluctuating Wind Pressures on 3D Square Cylinder by Unstructured-Grid LES Formulation of LES Using Unstructured Grid System for Wind-Resistant Design of Buildings (Part 1).” *Journal of Structural and Construction Engineering, Trans. AIJ* 687: 913-21. (in Japanese)

[18] Yoshikawa, M., and Tamura, T. 2016. “Wind Load Estimation of Vertical Fins on Walls of High-Rise Building Formulation of LES Using Unstructured Grid System for Wind-Resistant Design of Buildings (Part 3).” *J. Struct. Construct. Eng., Trans. AIJ* 722: 665-74. (in Japanese)

[19] Okuda, Y., and Taniike, Y. 1993. “Conical Vortices over Side Face of a Three-Dimensional Square Prism.” *Journal of Wind Engineering and Industrial Aerodynamics* 50: 163-72.